Journal of Power Sources 196 (2011) 7654–7664

Contents lists available at ScienceDirect

Journal of Power Sources

journal homepage: www.elsevier.com/locate/jpowsour

Two-dimensional model of distributed charge transfer and internal reforming within unit cells of segmented-in-series solid-oxide fuel cells

Huayang Zhu*, Robert J. Kee

Engineering Division, Colorado School of Mines, Golden, CO 80401, USA

ARTICLE INFO

Article history:
Received 10 January 2011
Received in revised form 8 April 2011
Accepted 13 April 2011
Available online 21 April 2011

Keywords:
SOFC
Modeling
Segmented in series
Distributed charge transfer
Internal reforming

ABSTRACT

This paper develops a computational model to represent details of reactive porous-media transport, elementary catalytic chemistry, and electrochemistry within unit cells of segmented-in-series solid oxide fuel cell (SIS-SOFC) modules. Because the composite electrode structures are thin (order of tens of microns), electrochemical charge-transfer chemistry can proceed throughout the composite electrode structures. Modeling such spatially distributed charge transfer is significantly more complex than modeling situations where the charge transfer can be represented at an interface between electrode and electrolyte. The present model predicts electric-potential fields of electrode and electrolyte phases, with the charge-transfer rates depending upon local electric-potential differences and the local gas-phase composition. The paper summarizes the underpinning physical and chemical models and uses examples to illustrate and interpret important aspects of SIS performance.

1. Introduction

Fig. 1 illustrates the layout of a segmented-in-series (SIS) solid-oxide fuel cell (SOFC) module in which planar SIS cells are arrayed as narrow strips on the outside of a porous support structure. Fuel flows inside the support and the cathode sides of the SIS are exposed to air on the outside. Each cell is composed of a membrane-electrode assembly (MEA) and an interconnect structure. The MEA consists of a cermet anode (e.g., Ni–yttria-stabilized zirconia, Ni–YSZ), dense electrolyte (e.g., YSZ), and composite cathode (e.g., strontium-doped lanthanum manganate–YSZ, LSM–YSZ). The cathode in the present study is a two-layer design using a pure LSM current collection layer above an LSM–YSZ functional layer. Each layer is usually a few tens of microns thick and the support structure is on the order of a millimeter thick. The width of each cell is typically on the order of a few millimeters. As illustrated here, a porous catalyst layer at the interface between the support structure and the fuel channel can promote reforming hydrocarbon fuels.

Oxygen ions O^{2-} are produced within the cathode by the electrochemical reduction of gas-phase oxygen, using electrons supplied from the anode of the neighboring cell. Electric current is produced along the width of the MEA as the oxygen ions that are transported across the dense electrolyte are electro-oxidized by the fuel H_2. Oxygen ions are transported across the dense electrolyte within the MEA, but the cells are isolated such that oxygen ions cannot be transported between cells. The inset in Fig. 1 shows that each cell is connected electrically in series with the lateral neighboring cells. The electrons produced within the anode of one cell are conducted into the cathode of the neighboring cell. Electric current from the anode interconnect at one end of the module is delivered to an external circuit, with electrons being returned to the cathode interconnect at the other end of the module. At the full system level, multiple modules can be connected electrically either in series or parallel.

1.1. Potential advantages of SIS

Segmented-in-series architectures offer several potential benefits. Electrical current is carried laterally through width of each cell, which can produce significant ohmic losses, especially in the cathode where the materials can have relatively high electrical resistance R. However, connecting many cells electrically in series builds up module voltage, thus reducing ohmic (I^2R) losses because the high voltage reduces current I for a certain electrical power. Overall cell performance benefits by reducing lateral electrical resistance, which is usually accomplished by using short cell widths. One objective of the present paper is to determine optimal cell widths.

The SIS approach confines Ni to the thin anode structure, thus reducing cost by significantly reducing the amount of Ni required in comparison to more common Ni–YSZ anode-supported SOFC architectures. The SIS supports do not carry electrical or ionic current, and thus can be fabricated from relatively low-cost materials such as partially stabilized zirconia (PSZ). The MEA layers can be fab-

* Corresponding author. Tel.: +1 303 273 3890; fax: +1 303 273 3602.
E-mail address: hzhu@mines.edu (H. Zhu).

0378-7753/$ – see front matter © 2011 Elsevier B.V. All rights reserved.
doi:10.1016/j.jpowsour.2011.04.023

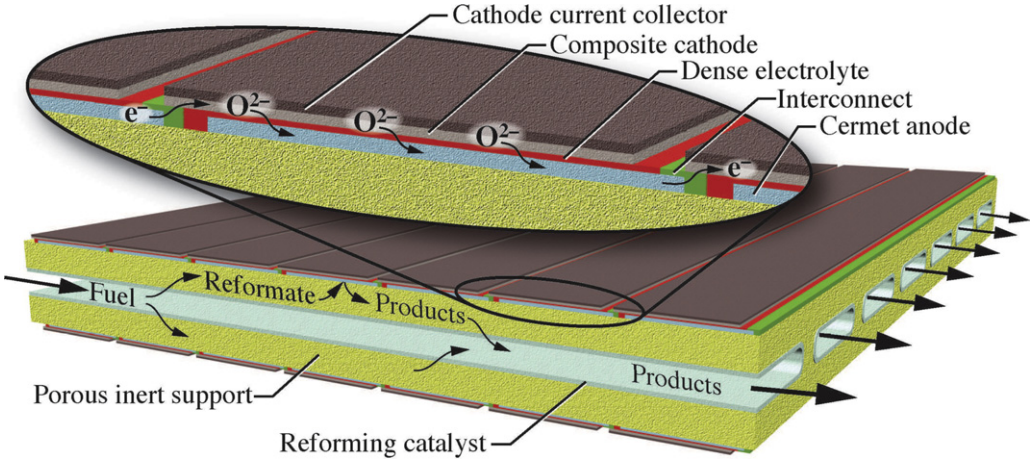

Fig. 1. Section of a segmented-in-series module.

ricated using relatively low-cost screen-printing technology. The model presented in this paper provides quantitative tool to assist evaluating design alternatives.

1.2. Prior literature

Alternative SIS-SOFC architectures have been studied since the mid 1960s [1–3]. Initial efforts considered cells that were applied as rings to the exterior of cylindrical porous support tubes. Later designs considered planar cells that were applied to flat porous support structures (e.g., Fig. 1). Mitsubishi Heavy Industries continues to develop SIS architectures on circular tubes [4] and Rolls-Royce is developing planar architectures [5,6]. Rolls-Royce uses the name Integrated Planar Solid Oxide Fuel Cell (IP-SOFC) to describe their design. Recently, Liu et al. have fabricated cone-shaped anode-supported SIS-SOFCs with good performance [7,8].

Barnett et al. have published a number of studies concerning system design and optimization [9–12]. Zhan and Barnett suggested using an inner reforming or partial-oxidation catalyst (as illustrated in Fig. 1) to enable the use of hydrocarbon fuels. The porous support structure also serves as a barrier layer that facilitates the use of hydrocarbon fuels without carbon deposits [13,14]. Based on modeling and experimental efforts, Barnett et al. have achieved high power density by reducing the lateral resistance losses across the electrodes and maintaining large active cell area through lowering the cell width and interconnect area [9,11,12]. Lai and Barnett [9] presented a model to analyze SIS performance as functions of cell and interconnect geometry, support material, cell area-specific resistance, and electrode sheet resistance. These results showed that power densities around 1 W cm^{-2} can be obtained using cell widths of about 1–2 mm. Lai and Barnett also reported that the cathode electrical resistance can be significantly reduced by applying a porous LSM current-collection layer above the cathode [11]. Using Ni–YSZ| YSZ|Pt–YSZ cells operating on humidified H_2 at 800 °C and atmospheric pressure, Pillai et al. [12] measured power densities of approximately 0.7 W cm^{-2} using cell widths of approximately 1.2 mm and interconnect widths of approximately 0.2 mm.

Haberman and Young have developed three-dimensional computational-fluid-dynamics (CFD) models to investigate the effects of fuel and air flow as well as heat and mass transport at the system level for IP-SOFC designs [15–17]. Several other groups have also developed planar SIS models that incorporate porous-media transport, coupled with reforming chemistry and electrochemistry [18,19]. Cui and Cheng developed two-dimensional axisymmetric models for the tubular SIS-SOFC to analyze the effects of the cell geometry on the electrical performance and species transport [20].

Compared to prior literature, the present model makes significant advances in the fundamental representation of chemistry and electrochemistry. Electric potentials for both ion- and electron-conducting phases are modeled throughout the entire cell. Hence, both ionic and electron fluxes are predicted throughout the system. Electrochemical charge-transfer chemistry depends on the local temperature, gas-phase composition, and electric-potential differences between phases. The spatial extent of the charge-transfer region depends on electrode structure, including primary particle sizes, phase densities, porosity, tortuosity, etc. Reactive porous-media gas-phase transport is represented using a Dusty-Gas model. The model also represents elementary catalytic chemistry (typically tens of elementary reactions) within the composite anode and within the catalytic layer at the interface between the fuel flow and the support structure. The elementary catalytic chemistry represents the internal reforming or partial oxidation of hydrocarbon fuels as well as other thermal chemistry such as water-gas-shift process.

2. Physical and chemical model

This paper focuses on the design and performance of individual unit cells, including the interconnect region and the underlying support structure. However, the fuel flow within the channels and the exterior air flow are not directly modeled. The model is formulated in terms of continuum differential equations that describe the electric potentials for the electrode and electrolyte phases as well as Faradaic charge transfer between phases. The porous-media transport of gases within the pore spaces is modeled with a Dusty-Gas model. Catalytic reforming and partial oxidation of fuels is based upon elementary reaction mechanisms.

Fig. 2 illustrates the structure of the unit cell, including nominal dimensions. The figure calls attention to a “unit width” and an “active width”. The unit width is the width of the cell repeating unit, which includes interconnect and cell-isolation features. The active width is the width over which the anode and cathode structures overlap. Electrical current is produced primarily within the active width. As illustrated in Fig. 2, the present paper considers the lateral widths of features within the interconnect regions to be fixed at 80 μm. Assuming a fixed interconnect structure, the model is used to determine unit width that maximizes cell performance.

Because the anode and cathode thicknesses are on the order of 50 μm, the electrochemical charge-transfer processes are likely to be distributed throughout most of the porous electrode structure [21]. Therefore, SIS models should accommodate charge-transfer electrochemistry throughout the MEA. Because a detailed discus-

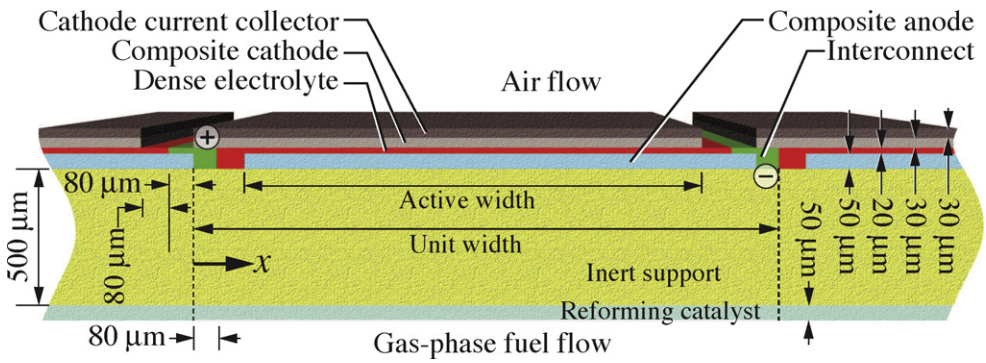

Fig. 2. Illustration of the MEA structure of the SIS unit cell, showing nominal physical dimensions.

sion of the distributed charge transfer model is provided elsewhere [21], the transport and chemistry theory is presented here in summary form.

2.1. Porous-media transport and chemistry

Chemically reacting gas-phase species transport through the porous electrodes is represented by species and overall mass-continuity equations as

$$\frac{\partial(\phi_g \rho Y_k)}{\partial t} + \nabla \cdot \mathbf{j}_k = W_k \dot{s}_k, \tag{1}$$

$$\frac{\partial(\phi_g \rho)}{\partial t} + \sum_{k=1}^{K_g} \nabla \cdot \mathbf{j}_k = \sum_{k=1}^{K_g} W_k \dot{s}_k. \tag{2}$$

The independent variables are time t and the spatial coordinates. The dependent variables are the gas-phase mass density ρ and the mass fractions Y_k. Other parameters include the porosity ϕ_g and species molecular weights W_k. Gas-phase species mass fluxes $\mathbf{j}_k$ through the porous structure are determined from the Dusty-Gas model (DGM) [22,23], which is an implicit relationship among the gas-phase species molar fluxes $\mathbf{J}_k$, molar concentrations $[X_k]$, concentration gradients, and the pressure gradient as

$$\sum_{\ell \neq k} \frac{[X_\ell]\mathbf{J}_k - [X_k]\mathbf{J}_\ell}{[X_T] D^e_{k\ell}} + \frac{\mathbf{J}_k}{D^e_{k,Kn}} = -\nabla[X_k] - \frac{[X_k]}{D^e_{k,Kn}} \frac{B_g}{\mu} \nabla p, \tag{3}$$

where μ is the mixture viscosity, $[X_T] = p/RT$ is the total molar concentration, p is pressure, and B_g the permeability. The mass fluxes $\mathbf{j}_k$ are related to the molar fluxes $\mathbf{J}_k$ as $\mathbf{j}_k = W_k \mathbf{J}_k$. This formulation considers molecular transport via ordinary and Knudsen diffusion as well as pressure-driven Darcy flow. The effective binary and Knudsen diffusion coefficients can be evaluated as

$$D^e_{k\ell} = \frac{\phi_g}{\tau_g} D_{k\ell}, \quad D^e_{k,Kn} = \frac{2}{3} \frac{r_p \phi_g}{\tau_g} \sqrt{\frac{8RT}{\pi W_k}}, \tag{4}$$

which are related to the ordinary multicomponent diffusion coefficients $D_{k\ell}$ via the porous-media microstructure, including average pore radius r_p and tortuosity τ_g. For the problems considered in the present paper, pressure gradients within the porous structures are very small, making the pressure-driven species transport negligible. Nevertheless, the full Dusty-Gas model is retained.

The molar production rates of gas-phase species due to heterogeneous thermal catalytic chemistry and electrochemical charge-transfer reactions are represented by $\dot{s}_k$. Because the temperatures are relatively low ($\approx$800 °C) and pore size within an electrode is comparable to the molecular mean-free-path length, homogeneous gas-phase kinetics can be neglected. The species production rates $\dot{s}_k$ are functions of temperature, gas composition, surface-species coverages, and electric-potential differences between the electrode and electrolyte phases. In addition to gas-phase species, the chemistry also depends upon surface-adsorbed species. The temporal variations of site coverages θ_k of surface-adsorbed species are represented as

$$\frac{d\theta_k}{dt} = \frac{\dot{s}_k}{\Gamma}, \quad (k = 1, \ldots, K_s), \tag{5}$$

where Γ is available site density and K_s is the number of the surface-adsorbed species. At steady state the net production rates of surface species vanish (i.e., $\dot{s}_k = 0$).

Heterogeneous reforming within the Ni–YSZ anode structure represented by an elementary reaction mechanism that incorporates steam and dry reforming as well as partial oxidation on the Ni surfaces [24,25]. The reaction mechanism also represents the important effects of water-gas-shift processes (globally, $H_2O + CO \rightleftharpoons H_2 + CO_2$). In addition to reforming within the Ni–YSZ anode, a Rh catalyst layer at the interface between the support structure and the fuel channel may be used to promote hydrocarbon reforming. The catalytic reforming of CH_4 on Rh is also represented by an elementary heterogeneous reaction mechanism [26].

2.2. Charge conservation

Charge transport and charge transfer both depend upon spatial electric-potential variations within the electron-conducting phase (i.e., the Ni phase in the anode and LSM in the cathode) and ion-conducting phase (i.e., the ceramic YSZ in the anode, cathode and electrolyte). Because the composite electrodes are thin, quantitative predictions require modeling electric-potential variations throughout the entire MEA. This is in contrast to modeling anode-supported cells, where it is sometimes appropriate to model the active charge-transfer region without spatial resolution at the interface between the composite anode and the dense electrolyte. In a Ni–YSZ| YSZ|LSM–YSZ MEA, three electric-potential fields are relevant. They are the electric potential for the electron-conducting phase within the composite anode Φ_a, the electric potential for the electron-conducting phase within the cathode Φ_c, and the electric potential for the electrolyte phase Φ_e, which spans the anode, dense electrolyte, and cathode. The three electric potentials are governed by charge-conservation equations. For steady-state operating conditions the charge-conservation equations may be stated as [21]

$$\nabla \cdot (\sigma^e_e \nabla \Phi_e) = \begin{cases} \dot{s}_{a,e} & \text{within anode} \\ 0 & \text{within electrolyte} \\ \dot{s}_{c,e} & \text{within cathode} \end{cases}, \tag{6}$$

$$\nabla \cdot (\sigma^e_a \nabla \Phi_a) = -\dot{s}_{a,e} \quad \text{within anode}, \tag{7}$$

$$\nabla \cdot (\sigma^e_c \nabla \Phi_c) = -\dot{s}_{c,e} \quad \text{within cathode}. \tag{8}$$

In these equations σ_a^e and σ_c^e, are the effective conductivities of the electron-conducting phases within the composite anode (i.e. Ni) and cathode (i.e., LSM), respectively. The effective ion conductivity for the ion-conducting phase (i.e., YSZ) is σ_e^e. The effective conductivities of the composite electrodes can be significantly different from the pure material properties. Generally speaking the ion conductor, the electron conductor, and the pores each occupy approximately one third of the composite structure. Thus, on a simple geometric basis, one expects that the effective conductivity to be no greater than one third of the pure material conductivity. Because of necking between particles, particle–particle interface resistances, tortuous conduction paths, and material inhomogeneities such as grain boundaries, the effective conductivities are usually much lower than might be expected by considering the phase volume alone. Effective properties can be estimated using percolation theory [27] and derived from detailed simulations of synthesized microstructures [28].

Electrochemical transfer of charge between phases affects the electric potentials within the phases. In the continuum conservation equations the net charge-transfer rates are represented as source terms on the right-hand sides of Eqs. (6)–(8). The nomenclature $\dot{s}_{m,e}$ has the meaning that the phase m may be either the anode "a" or the cathode "c." Charge-transfer reactions usually involve both charged and uncharged species. The second subscript "e" in $\dot{s}_{m,e}$ indicates the transfer of electrons, which are the only rates that are directly relevant to the charge-conservation equations. A positive value of $\dot{s}_{m,e}$ indicates the transfer of negative charge into phase m, which tends to decrease the electric potential of the phase. Note that the charge-transfer source terms appear in the charge-conservation equations for both participating phases, but with opposite signs. That is, all the charge that leaves one phase enters the partner phase. Further details about the charge-transfer formulation is found in Zhu and Kee [21].

2.3. Butler–Volmer kinetics

Within a composite electrode (e.g., Ni–YSZ anode or LSM–YSZ cathode) the overall charge-transfer processes involve a complex interaction of thermal chemistry and electrochemistry. Even hydrogen electro-oxidation within a Ni–YSZ anode can involve a complex set of elementary reactions [29–33]. The present paper represents charge-transfer kinetics in a Butler–Volmer form that is derived from elementary reactions [23,32].

Within the Ni–YSZ anode, H_2 is assumed to be the only electrochemically active fuel. Although the fuel stream may contain CO and methane, the catalytic reforming and water-gas-shift processes are dominant in the production of H_2. The electrochemical oxidation of H_2 within the Ni–YSZ anode and O_2 reduction within the LSM–YSZ cathode can be represented globally as

$$H_2(g) + O^{2-}(el) \leftrightharpoons H_2O(g) + 2e^-(a), \tag{9}$$

$$(1/2)O_2(g) + 2e^-(c) \leftrightharpoons O^{2-}(el), \tag{10}$$

where $O^{2-}(el)$ are oxygen ions within the ionic-conducting electrolyte phase, $e^-(a)$ are the electrons within the electronic-conducting anode phase, and $e^-(c)$ are the electrons within the electronic-conducting cathode phase. In Butler–Volmer form the charge-transfer rates (i.e., current density $i_{BV,e}$) can be expressed in terms of the local activation overpotential η_{act} as

$$i_{BV,e} = i_0 \left[\exp\left(\frac{\alpha_a F \eta_{act}}{RT}\right) - \exp\left(-\frac{\alpha_c F \eta_{act}}{RT}\right)\right], \tag{11}$$

where i_0 is the exchange current density, α_a and α_c are anodic and cathodic symmetry factors. The first term in the square brackets represents the anodic current density (producing electrons) and the second term represents the cathodic current density. At equilibrium electric potential, the chemistry proceeds at equal and opposite rates in the anodic and cathodic directions. The Butler–Volmer expression describes the net rate of a reversible reaction. The exchange current density represents the magnitude of the equal and opposite current densities at equilibrium electric potential. The value of i_0 depends upon the length of three phase boundary, the effectiveness of electrocatalyst, the temperature, and the activities of the participating species. Because the Butler–Volmer formulation represents a global charge-transfer process, the symmetry factors α are not the same as they would be for an elementary reaction. Moreover, $\alpha_a + \alpha_c \neq 1$ as would be the case for an elementary reaction.

The activation overpotential η_{act} is defined as

$$\eta_{act} = E_a - E_a^{eq} = (\Phi_a - \Phi_e) - (\Phi_a - \Phi_e)^{eq}. \tag{12}$$

That is, $E_a = (\Phi_a - \Phi_e)$ is the electric-potential difference between the electrode phase and the electrolyte phase, and $E_a^{eq} = (\Phi_a - \Phi_e)^{eq}$ is the electric-potential difference that causes the charge-transfer reaction to be equilibrated (i.e., proceeding in the anodic and cathodic directions at equal and opposite rates).

Zhu et al. [23,21,32] developed expressions for the anode and cathode exchange current densities as

$$i_{0,H_2} = i^*_{H_2} \frac{(p_{H_2}/p^*_{H_2})^{(1-\alpha_a/2)} (p_{H_2O})^{\alpha_a/2}}{1 + (p_{H_2}/p^*_{H_2})^{1/2}}, \tag{13}$$

$$i_{0,O_2} = i^*_{O_2} \frac{(p_{O_2}/p^*_{O_2})^{\alpha_a/2}}{1 + (p_{O_2}/p^*_{O_2})^{1/2}}, \tag{14}$$

where the gas-phase partial pressures p_k are measured in atmospheres. Zhu, et al. derive expressions for the factors $p^*_{H_2}$ and $p^*_{O_2}$, which depend upon heterogeneous adsorption and desorption rates [23].

Temperature dependencies for the exchange current densities are expressed as

$$i^*_{H_2} = i^*_{ref,H_2} \exp\left[-\frac{\hat{E}_{a,H_2}}{R}\left(\frac{1}{T} - \frac{1}{T_{ref}}\right)\right], \tag{15}$$

$$i^*_{O_2} = i^*_{ref,O_2} \exp\left[-\frac{\hat{E}_{a,O_2}}{R}\left(\frac{1}{T} - \frac{1}{T_{ref}}\right)\right], \tag{16}$$

where $\hat{E}_{a,k}$ is activation energies, and the parameter $i^*_{ref,k}$ is assigned empirically to fit measured polarization data at the reference temperature T_{ref}.

The spatially varying local electric-potential differences within the porous anode and cathode structures are defined as

$$E_a = \Phi_a - \Phi_{e,a}, \quad E_c = \Phi_c - \Phi_{e,c}, \tag{17}$$

where $\Phi_{e,m}$ represents the electrolyte-phase electric potential in the composite anode "a" or cathode "c". The local electric potential fields are obtained directly from the solutions to Eqs. (6)–(8). The activation overpotentials in Eq. (11) for the anode and cathode are defined as

$$\eta_{act,a} = E_a - E_a^{eq}, \quad \eta_{act,c} = E_c - E_c^{eq}, \tag{18}$$

which depend upon the local equilibrium electric-potential differences E_a^{eq} and E_c^{eq}. Assuming bulk O^{2-} concentration within the YSZ lattice is spatially uniform throughout the MEA structure, E_a^{eq} and E_c^{eq} can be evaluated as [21]

$$E_a^{eq} = \frac{\mu^\circ_{H_2O} - \mu^\circ_{H_2}}{2F} + \frac{RT}{2F} \ln \frac{p_{H_2O,a}}{p_{H_2,a}}, \tag{19}$$

$$E_c^{eq} = \frac{\mu^\circ_{O_2}}{4F} + \frac{RT}{4F} \ln p^{1/2}_{O_2,c}. \tag{20}$$

where μ_k° are standard-state chemical potentials and p_k are the local gas-phase partial pressures (in atmospheres).

2.4. Boundary conditions

Boundary and interface conditions are required to solve the coupled system of Eqs. (1), (2) and (6)–(8). Fig. 3 illustrates the numerous boundary and interface conditions that must be imposed throughout the multicomponent cell structure.

At the interface with the fuel and air compartments the gas-phase composition is assumed to be that within either the bulk fuel or air flow. At the interface between the cathode and the air compartment the ionic fluxes vanish (i.e., $\mathbf{n}\cdot\sigma_e^e\nabla\Phi_e = 0$) and the cathode electric potential Φ_c can be set to be a reference electric potential as Φ_c°. At the interface between the anode and the fuel compartment the ionic fluxes vanish (i.e., $\mathbf{n}\cdot\sigma_e^e\nabla\Phi_e = 0$), and the anode electric potential Φ_a can be specified as Φ_a°. The operating cell potential is $E_{cell} = \Phi_c^\circ - \Phi_a^\circ$. The electron flux at the interface between the composite electrode structures and the dense electrolyte must vanish (i.e., $\mathbf{n}\cdot\sigma_a^e\nabla\Phi_a = 0$, and $\mathbf{n}\cdot\sigma_c^e\nabla\Phi_c = 0$) because the dense electrolyte membrane is assumed to be a purely ionic conductor.

3. Numerical algorithm

The governing conservation equations form a coupled system of nonlinear partial-differential equations. The independent variables are the spatial coordinates and the dependent variables are the gas-phase density ρ_g, mass fractions Y_k ($k = 1, \ldots, K_g$), surface coverages θ_k ($k = 1, \ldots, K_s$), electric potentials Φ_m within the electrode and electrolyte phases. The entire cell and support structure is discretized using a finite-volume representation on a cartesian mesh. Component-specific material properties and reaction chemistries are used within each of the components.

An operator-decomposition technique is used to decouple the gas-phase transport and reaction processes. The numerical solution is obtained by solving sequentially and iteratively three submodels: (1) the electric-potential distributions, (2) the gas-phase species transport within the porous electrodes, and (3) the chemical and electrochemical reactions. The resulting system of nonlinear algebraic equations is solved with a modified Newton iteration, with a preconditioned Krylov subspace iteration used to solve the linearized algebraic equations [34].

The chemical kinetics, which does not involve spatial operators, is evaluated within each finite volume by a time-relaxation algorithm, using LIMEX to solve the differential-algebraic equations [35]. Thermodynamic properties, transport properties, and reaction chemistry are managed using the CHEMKIN software [36].

4. Results and discussion

The present study considers an SIS architecture with specific component thicknesses and interconnect structures, but with different unit-cell widths. As introduced in Fig. 2 physical dimensions are as follows. The composite cathode consists of two layers – a 30 μm LSM–YSZ functional layer adjacent to the dense electrolyte layer and a 30 μm LSM layer to increase the lateral electronic conduction. The dense YSZ electrolyte membrane is 20 μm thick and the composite Ni–YSZ anode is 50 μm thick. The MEA structure rests on a support layer, that is composed of 450 μm of a porous chemically inert structure above a Rh catalyst layer that is 50 μm thick. The electronically conducting interconnect is an L-shaped structure that consists of two 80 μm wide segments. Because the interconnect must survive in both oxidizing and reducing environments, materials selection is limited. One viable choice is strontium-doped lanthanum chromite (LSC), but it has low electronic conductivity ($\sigma < 1\ S\,cm^{-1}$). The lateral isolation gap between cathodes is 160 μm wide, spanning 80 μm of interconnect and 80 μm of dense electrolyte. Reducing the widths of these 80 μm spaces would be functionally beneficial. However, dimensions smaller than 80 μm may be difficult to fabricate reliably with technology such as screen-printing.

The nominal unit-cell width in the present study is taken to be 1900 μm, with the active width (i.e., width over which the cathode and anode are both in direct contact with the dense electrolyte) being 1500 μm. A particular objective of the paper is to evaluate cell performance as a function of varying unit-cell active width.

Table 1 summarizes the physical dimensions and provides numerous other physical parameters and properties. In all cases the cathode is exposed to air at atmospheric pressure. However, two fuel streams are considered: (1) humidified H_2 (3% H_2O) and (2) a mixture resulting from partial steam reforming of CH_4. The cell is assumed to be operated isothermally 800 °C. Two cell operating potentials are considered: $E_{cell} = 0.50$ V and $E_{cell} = 0.75$ V. The cell potential E_{cell} is defined to be the difference between the cathode interconnect potential (left side of unit cell) and the anode interconnect (right side of the unit cell).

Table 1
Nominal physical parameters.

Parameters	Value	Units
Anode, Ni–YSZ		
Thickness (L_a)	50	μm
Porosity (ϕ_g)	0.35	
Ni volume fraction (ϕ_{Ni})	0.23	
YSZ volume fraction (ϕ_{YSZ})	0.42	
Tortuosity (τ_g)	4.5	
Ni particle radius (r_{Ni})	0.5	μm
YSZ particle radius (r_{YSZ})	0.5	μm
Specific catalyst area (A_s)	1000	cm^{-1}
Exchange current factor (i^*_{ref,H_2})	48,000	$A\,cm^{-3}$
Activation energy ($\hat{E}_{a,H_2}$)	120	$kJ\,mol^{-1}$
Reference temperature (T_{ref})	800	°C
Anodic symmetry factor (α_a)	1.5	
Cathodic symmetry factor (α_c)	0.5	
Cathode, LSM–YSZ		
Thickness (L_c)	60	μm
Porosity (ϕ_g)	0.35	
LSM volume fraction (Φ_{LSM})	0.31	
YSZ volume fraction (Φ_{YSZ})	0.34	
Tortuosity (τ_g)	4.00	
LSM particle radius (r_{LSM})	0.625	μm
YSZ particle radius (r_{YSZ})	0.625	μm
Exchange current factor (i^*_{ref,O_2})	7200	$A\,cm^{-3}$
Activation energy ($\hat{E}_{a,O_2}$)	130	$kJ\,mol^{-1}$
Reference temperature (T_{ref})	800	°C
Anodic symmetry factor (α_a)	0.55	
Cathodic symmetry factor (α_c)	0.45	
Electrolyte, YSZ		
Thickness (L_{el})	20	μm
Anode support diffusion layer		
Thickness (L_{ad})	450	μm
Porosity (ϕ_g)	0.35	
Tortuosity (τ_g)	4	
Solid volume fraction (ϕ_s)	0.65	
Solid particle radius (r_s)	0.75	μm
Interconnect (LSC)		
Electrical conductivity (σ_{LSC})	1	$S\,cm^{-1}$
Anode support Rh catalyst layer		
Thickness (L_{ac})	50	μm
Porosity (ϕ_g)	0.35	
Tortuosity (τ_g)	4	
Solid volume fraction (ϕ_s)	0.65	
Solid particle radius (r_s)	0.75	μm
Specific catalyst area (A_s)	1000	cm^{-1}

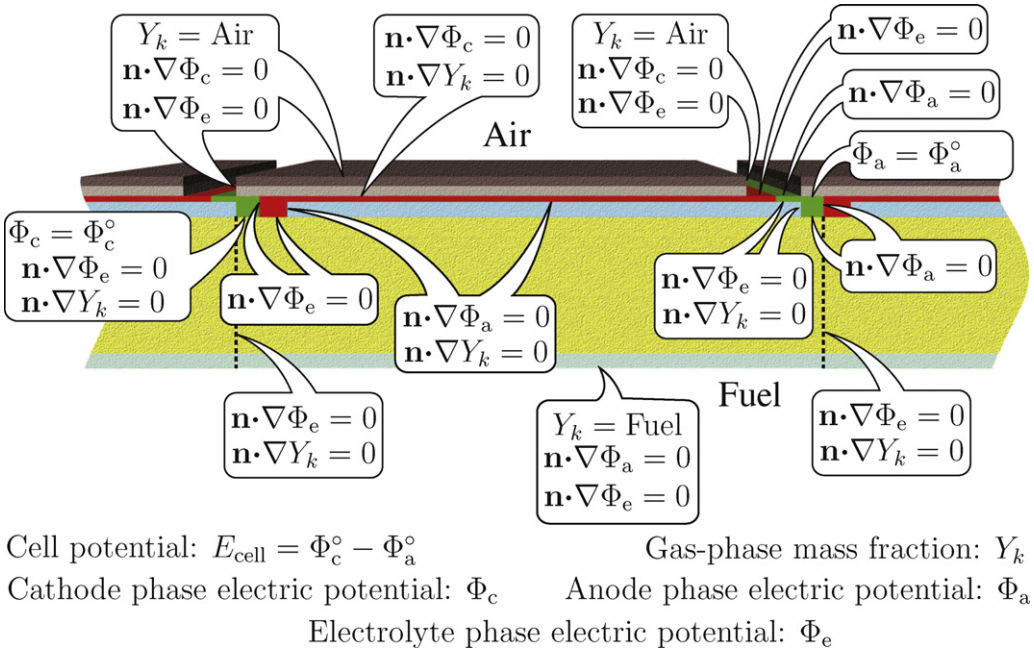

Fig. 3. Boundary and interface conditions throughout the MEA unit cell.

4.1. Characterization of a unit cell

Consider first a fuel that is the result of equilibrium reformation of an initial mixture of 60% CH_4 and 40% H_2O at 800 ° C and atmospheric pressure. Specifically, the fuel is a mixture of 66.1% H_2, 21.8% CO, 11.6% CH_4, 0.3% H_2O, and 0.2% CO_2.

It may be noted that the gas composition flowing into the SOFC fuel channel could be such that carbon deposits would be formed, especially on Ni. However, the SIS architecture (Fig. 1) provides certain advantages that counteract the propensity for coking. The chemically inert porous support structure acts as a barrier layer [13,14] that impedes the transport of electrochemically generated H_2O from the Ni–YSZ anode and impedes the transport of hydrocarbons toward the anode. Thus, the gas mixture within the Ni–YSZ anode is less likely to coke than would be the gas composition the flow channel.

Using the nominal cell dimensions and material properties (Table 1), Fig. 4 shows predicted gas-phase mole-fraction (percent) contours within the pore volumes of the anode and support layers. Qualitatively, the concentrations of fuel species (i.e., H_2, CO, and CH_4) decrease from their mole fractions within the fuel channel toward the anode structure where they are consumed. The concentrations of product species (i.e., H_2O and CO_2), which are generated within the anode, decrease as they are transported toward the fuel channel. Concentration gradients are much higher within the catalytically active anode layer than they are in the chemically inert support structure. Because the fuel mixture is already at equilibrium composition and the Rh catalyst layer is only 50 μm thick, the catalyst layer has little influence.

Over much of the anode-layer width the species contours remain nearly parallel. In other words, the chemistry and transport within much of the MEA is nearly one-dimensional in the direction normal to the dense electrolyte layer. However, near the interconnect region, where electrochemistry is not active, significant two-dimensional behavior is evident. Geometric design and materials selection within the interconnect region is one of the more challenging aspects of SIS development.

Electrochemical variations in the interconnect region affect the species fields within the support structure. By assumption, the species fluxes within the support structure vanish at the interfaces between the upstream and downstream unit cells. Because fuel is consumed along the length of the fuel channels, this assumption is not strictly valid. However, the zero-flux assumption at the unit-cell boundaries is a reasonable approximation. With small unit-cell widths (e.g., 1900 μm), relatively little electrical power is generated within each unit cell. Consequently, relatively little fuel is consumed and products generated within each unit cell. Within a unit cell, the largest species fluxes between the MEA and the fuel channel are near the center of the support structure.

In addition to species contours, Fig. 4 also shows electric-potential contours within the electrolyte phase (YSZ) and electron pathlines within the electron-conducting phases (Ni and LSM) throughout the MEA structure. As with the species contours, the electric-potential contours are nearly one-dimensional over much of the MEA width. Most of the electric-potential variation is across the thickness of the dense-electrolyte layer. The concentration of electron pathlines in the LSM current-collection layer is the result of higher electrical conductivity in that layer compared to the underlying LSM–YSZ active cathode. Improving lateral conduction within the cathode structure is an important consideration in improving overall cell performance. Note that the electron pathlines do not cross the dense electrolyte, which is a pure oxygen-ion conductor. Rather, electrons are consumed by oxygen electro-reduction on the cathode side and produced by electro-oxidation of the fuel on the anode side.

4.1.1. Transverse profiles

Fig. 5 shows profiles of electric potentials and current densities through the MEA structure at three lateral positions (165 μm, 900 μm, and 1500 μm). In all cases the cell is operating at $E_{\text{cell}} = 0.75$ V. The graphs are oriented such that the anode is on the left and the cathode is on the right. Consider first Fig. 5a, showing electric potential profiles. The solid lines represent the electrode phases (Ni and LSM) and the dashed lines represent the electrolyte phase (YSZ). The electric-potential profiles are nearly overlapping, indicating approximately one-dimensional behavior. The electrode electric potential is nearly uniform within the Ni at $\Phi_a \approx -0.12$ V and within the LSM at $\Phi_c \approx 0.78$ V. With $E_{\text{cell}} = 0.75$ V, the anode

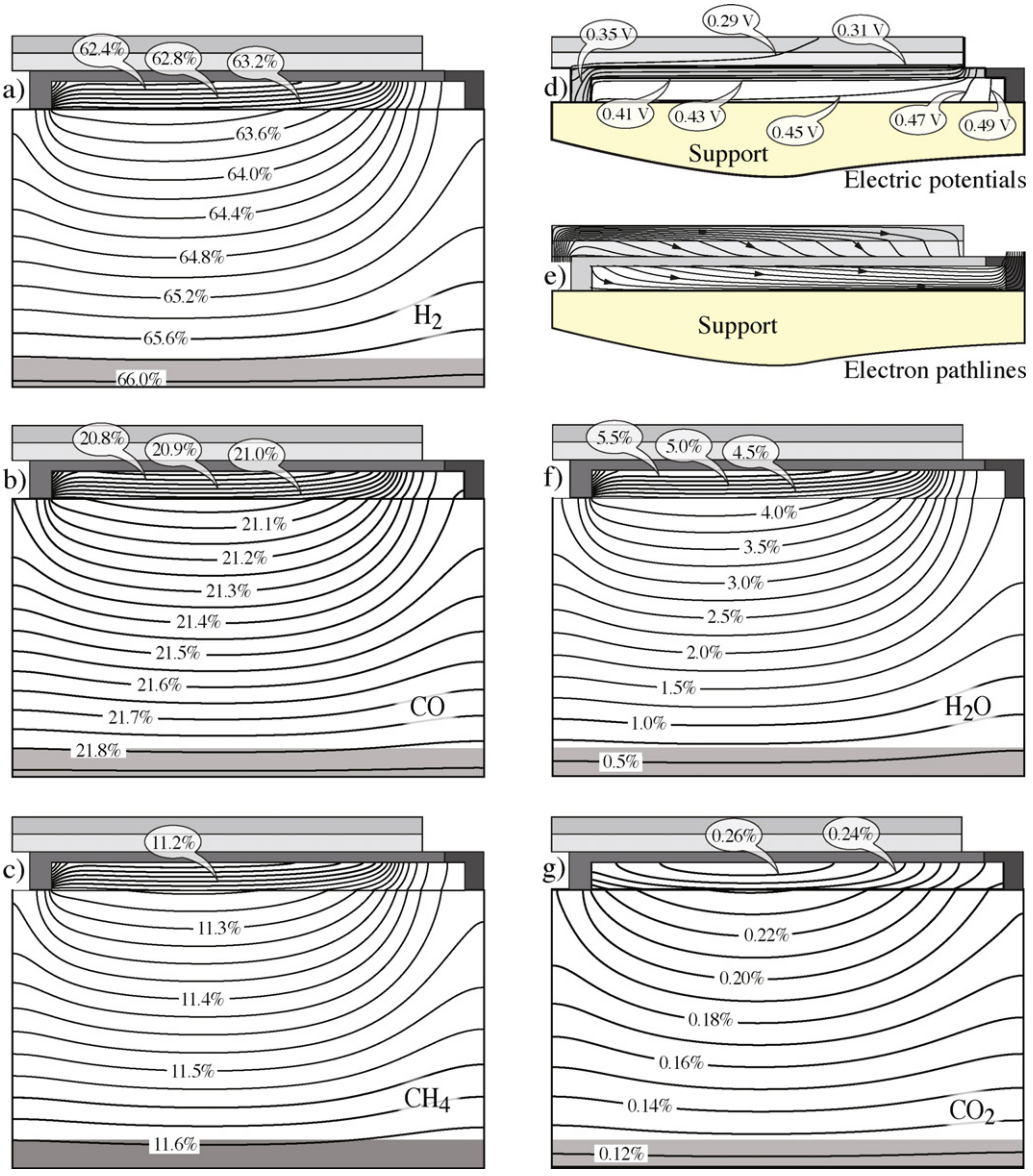

Fig. 4. Contour maps of gas-phase species mole fractions within the anode and support layers. Electric-potential contours within the electrolyte (YSZ) phase through the MEA structure. Electron path lines through the anode, cathode and interconnect structures. To assist visualization the vertical direction is expanded by a factor of two.

interconnect is fixed at $\Phi_a = 0$ V and the cathode interconnector is at $\Phi_c = 0.75$ V. The fact that the electrode electric-potential difference is greater than E_{cell} (i.e., the difference in interconnect potentials) is the result of the electric-potential gradients that are required to support lateral current flux.

Within the LSM–YSZ cathode, the electric potentials of both the cathode phase Φ_c and electrolyte phase Φ_e increase from the cathode–air interface toward the interface between the cathode and the dense electrolyte. Both the negatively charged ions and electrons are being transported from the cathode–air interface toward the interface between the cathode and the dense electrolyte. Such charged-species transport proceeds in the direction of the negative electrochemical-potential gradient. In other words, the negatively charged species generally are transported up the electric-potential gradient (i.e., from regions of relatively more negative electric potential toward regions of relatively more positive electric potential). The electric potential of the electrode phase (LSM) is always positive relative to the electric potential of the electrolyte phase (YSZ). That is local double layers between electrode and electrolyte phases are such that $\Delta\Phi = \Phi_{LSM} - \Phi_{YSZ} > 0$. The magnitude of the double layer (i.e., $\Delta\Phi$) is less positive near the dense-electrolyte interface than it is deeper into the cathode structure. Consequently, the cathodic charge-transfer rate is highest near the dense-electrolyte interface. As the magnitude of $\Delta\Phi$ decreases (i.e., the YSZ particles become relatively more positive) the rate of the charge-transfer reaction (globally $(1/2)O_2$ (g) + 2 e^- (LSM) $\rightleftharpoons O^{2-}$ (YSZ)) increases (Fig. 5b). This can be understood qualitatively in the sense that as the strength of the double layer decreases, it becomes easier to transfer negative charge from the electrode into the relatively more negative electrolyte. Within the cathode structure, the activation overpotential is always negative. In the context of the Butler–Volmer equation, a negative overpotential drives the charge-transfer reaction in the cathodic direction (i.e., consuming electrons).

The electric-potential profiles within the composite anode increase slightly from the interface between the anode and the dense electrolyte interface toward the interface between the anode and support structure. As in the cathode, negatively charged ions and electrons are transported up the electric-potential gradients. However, because the Ni electrical conductivity is so high, the

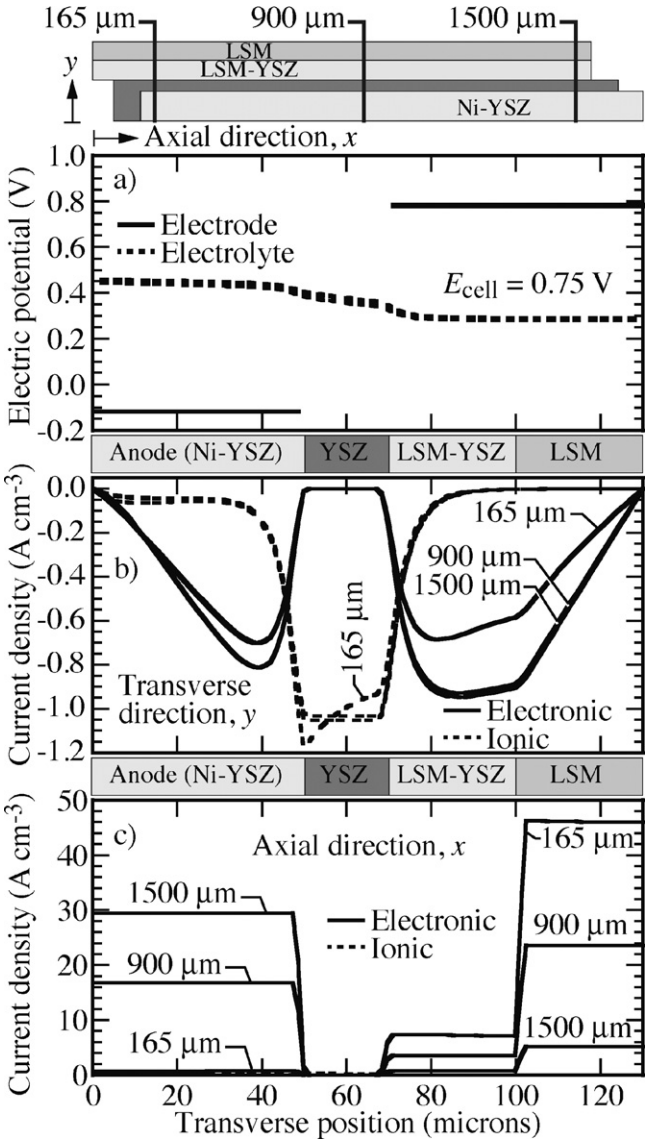

Fig. 5. Solution profiles of the electric potentials, electronic and ionic current fluxes in the lateral and vertical directions across the MEA unit cell at lateral positions of 165 μm, 900 μm, and 1500 μm.

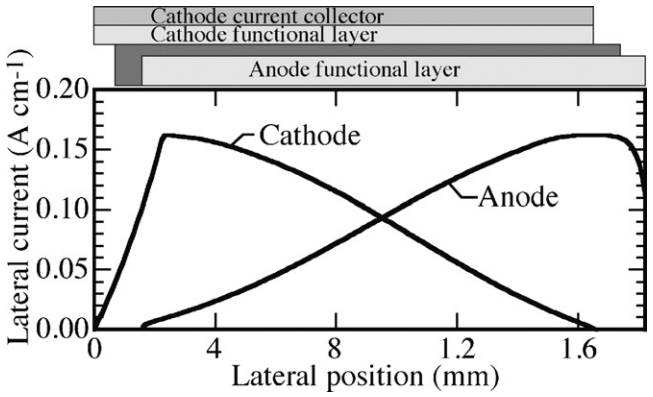

Fig. 6. Lateral current (x direction, per unit depth) along the width of the MEA.

electric-potential gradient within the anode phase is very small. Because the oxygen-ion flux is dominantly in the direction normal to the dense electrolyte, the lateral electric-potential gradient within the electrolyte phase (YSZ) is also small. Upon transferring charge from the oxygen ion in the YSZ phase to an electron in the Ni phase, the Ni provides a low-resistance path for electron flux toward the anode interconnect.

The electrode (Ni) electric potential is always lower than the electrolyte (YSZ) potential, and the overpotential is always positive. That is, the double layer within the anode is such that $\Delta\Phi = \Phi_{Ni} - \Phi_{YSZ} < 0$, with the electric-potential difference becoming less negative near the dense electrolyte interface. Consequently, the anodic charge-transfer rate is the highest near the dense-electrolyte interface. As the magnitude of $\Delta\Phi$ decreases (i.e., the YSZ particles become less positive) the rate of the charge-transfer reaction (globally, $H_2\,(g) + O^{2-}\,(YSZ) \rightleftharpoons H_2O\,(g) + 2e^-\,(Ni)$) increases (Fig. 5b). This behavior can be understood qualitatively in the sense that as the strength of the double layer decreases, the barrier to the transfer of negative charge into the negative electrode is reduced.

Within the dense electrolyte, there is no need to consider the electronic-conducting electric potential because the YSZ is a pure ionic conductor. As illustrated in Fig. 5a, the ion-conducting electric-potential profile within the dense electrolyte is linear. However, the oxygen-ion flux, which is proportional to the electric-potential gradient and the ion conductivity, varies vertically within the dense-electrolyte region (Fig. 5b).

Fig. 5c illustrates the electronic current density in the lateral direction across the width of the MEA unit cell. Because the dense YSZ membrane layer is a pure ionic conductor, the electronic current density vanishes within the dense YSZ layer. Fig. 5c shows that the variation in lateral electronic current density through the anode thickness is very small. On the cathode side, however, the lateral electronic current density within the LSM current-collection layer is much higher than it is in the LSM–YSZ layer. Fig. 5c also shows that lateral current density decreases on the cathode side from the lateral position of 165 μm toward 1500 μm, and increases correspondingly at the anode side.

4.1.2. Net lateral current

As illustrated in Fig. 4, the distribution of the electrolyte-phase electric potential and the pathlines of the electron current fluxes within the electrodes indicate that the electron fluxes within the anode and the cathode are oriented largely in lateral direction, and the ion flux through the dense electrolyte is oriented nearly perpendicular to the electrolyte interfaces with the composite electrode structures. However, Fig. 4 does not show quantitatively the electron and ion fluxes, both of which are vectors. The net electrical currents flowing laterally within the anode and cathode structures: $I_{a,x}$ and $I_{c,x}$ are defined to illustrate the quantitative variation of the electronic fluxes as follows

$$I_{a,x} = \int_{L_a} i_{a,x}\,dy, \tag{21}$$

$$I_{c,x} = \int_{L_c} i_{c,x}\,dy, \tag{22}$$

where $i_{a,x}$ and $i_{c,x}$ are the lateral components of the electronic current density $\mathbf{i}_m$ (m = a or c) and L_a and L_c are thickness of the anode and cathode layers, respectively. The local electron and ion current densities can be calculated from the electric-potential gradients as

$$\mathbf{i}_m = -\sigma_m^e \nabla\Phi_m. \tag{23}$$

Fig. 6 shows the net lateral electric-current fluxes (per unit depth of the cell, A cm^{-1}) within both electrodes. Electric current enters through the cathode interconnect and leaves through the anode interconnect. As shown in Fig. 4, current enters the cathode interconnect vertically, then turns to the lateral direction. Thus,

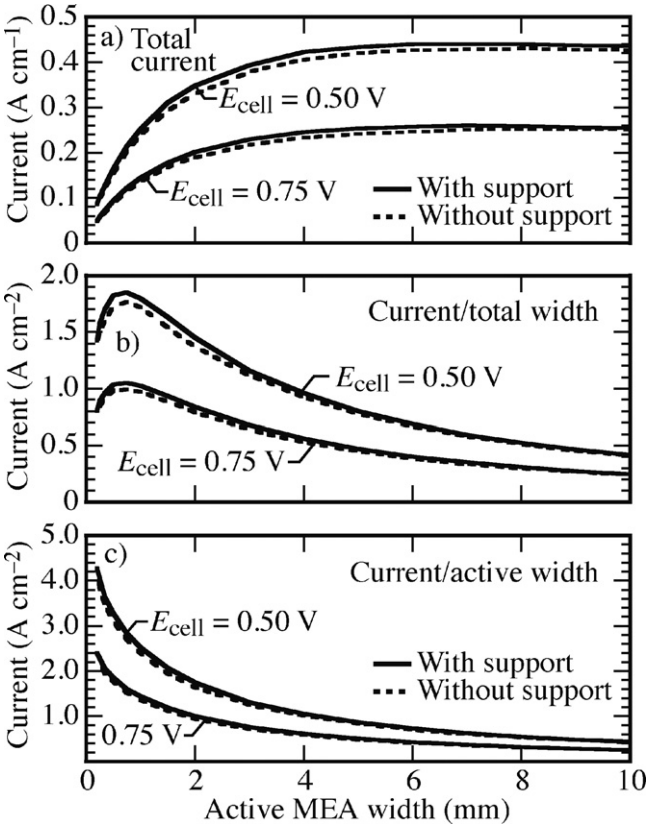

Fig. 7. Profiles of net current (top panel), current densities normalized by the overall width of the unit cell (middle panel) and current density normalized by the active length of the SIS unit cell (bottom panel) as functions of unit-cell active width. The results show two cell voltages, with and without the support structure in place. The interconnect material has a low electric conductivity of $\sigma = 1\ \mathrm{S\,cm^{-1}}$.

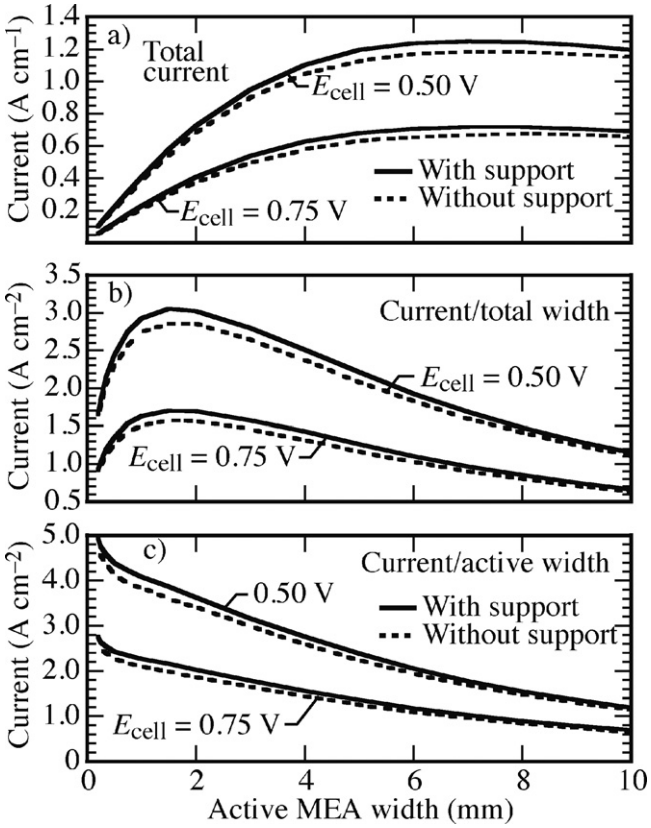

Fig. 8. Profiles of net current (top panel), current densities normalized by the overall width of the unit cell (middle panel) and current density normalized by the active length of the SIS unit cell (bottom panel) as functions of unit-cell active width. The results show two cell voltages, with and without the support structure in place. The interconnect material has a high electric conductivity of $\sigma = 5 \times 10^4\ \mathrm{S\,cm^{-1}}$.

the net lateral electrical current increases near the cathode interconnect. In the active MEA region, the electron current within the cathode is converted into the ionic current, which flows through the dense electrolyte, and then is converted into electron current within the anode. Because the ion current through the dense electrolyte is nearly uniform (Fig. 5b), the lateral electric-current profiles are nearly linear within the active MEA regions of the electrodes (Fig. 6). For this particular example, the net current developed by the unit cell is about $0.16\ \mathrm{A\,cm^{-1}}$. With the cell operating at $E_{cell} = 0.75$ V, the net power from the cell is approximately $0.12\ \mathrm{W\,cm^{-1}}$ (per unit depth of the cell).

The electric conductivity of the interconnect structure can greatly affect the cell performance. Because the interconnect material must be stable in both oxidizing and reducing atmospheres, the materials choices are limited. One viable choice is an electrically conducting doped perovskite (e.g., strontium-doped lanthanum chromite, LSC). However, because such materials have relatively low electrical conductivity ($\sigma < 1\ \mathrm{S\,cm^{-1}}$), there can be a significant voltage drop across the interconnect. All the electrical current produced by the roughly 1500 μm width of the active cell must be channeled through the relatively small interconnect structure. This current concentration can potentially cause local heating, or other possibly deleterious effects on the cell materials. The design of the interconnect regions and material choices are important to cell reliability and lifetime. Figs. 7 and 8 show results of a study considering the effects of increasing interconnect electrical conductivity.

4.2. Cell optimization

Because current in the SIS cell is flowing laterally, the lateral width of the SIS unit cell and the electric conductivity of the interconnect play important roles in cell performance. Consider all geometric and physical properties to be fixed except the unit-cell active width, which is varied from 0.2 mm to 10 mm. For these comparisons the fuel is taken to be 97% H_2 and 3% H_2O. Fig. 7 illustrates three measures of cell performance. First is the total current (per unit depth), second is the current density normalized by total width of the unit cell, and third is the current density normalized by the active width of the unit cell.

The total current generated by the unit cell can be evaluated as

$$I = \int_{\mathrm{CI}} i_{\mathrm{a},y}\,dx, \tag{24}$$

where "CI" is the cathode–interconnect interface area, and $i_{\mathrm{a},y}$ is the electronic current density in the vertical direction at the cathode–interconnect interface, and can be estimated based on the electric potential gradient within the interconnect. The current density per active width of the SIS unit cell can be defined as,

$$i_{\mathrm{active}} = \frac{I}{W_{\mathrm{active}}}, \tag{25}$$

where W_{active} is the active width of the SIS unit cell (Fig. 2). Similarly, the current density per total width of the unit cell is defined as

$$i_{\mathrm{total}} = \frac{I}{W_{\mathrm{total}}}, \tag{26}$$

where W_{total} is the full unit-cell width (including the interconnect structure).

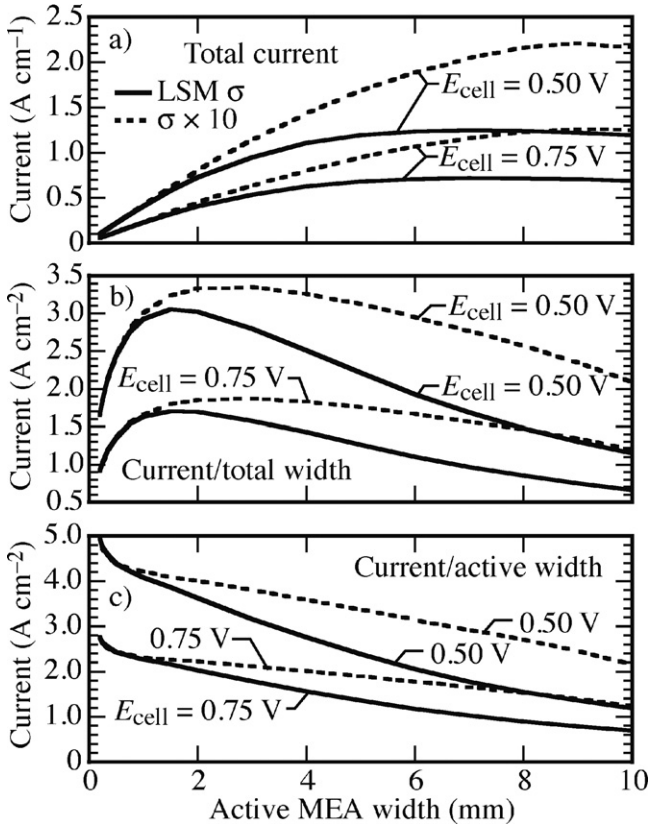

Fig. 9. Profiles of net current (top panel), current densities normalized by the overall width of the unit cell (middle panel) and current density normalized by the active length of the SIS unit cell (bottom panel) as functions of unit-cell active width. The results show the effect of increasing electrical conductivity of the LSM current-collection layer by a factor of 10. Two operating voltages are shown.

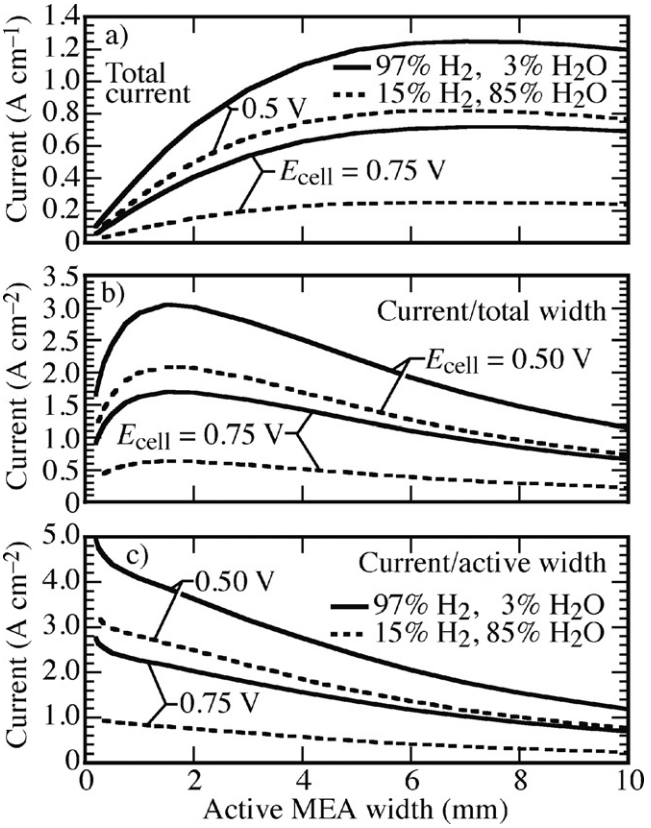

Fig. 10. Profiles of net current (top panel), current densities normalized by the overall width of the unit cell (middle panel) and current density normalized by the active length of the SIS unit cell (bottom panel) as functions of unit-cell active width. A fuel composition of 15% H_2 and 85% H_2O is compared with a fuel composition of 97% H_2 and 3% H_2O. Two operating voltages are shown.

4.2.1. Interconnect conductivity

Fig. 7 compares I, i_{active}, and i_{total} as functions of the unit-cell active width at two operating cell voltages (E_{cell} = 0.5 V and E_{cell} = 0.75 V), with and without the support structure in place. In this case an interconnect with low electrical conductivity, such as LSC, is used (σ = 1 S cm^{-1}). Fig. 7a shows that the total current I (per unit depth) achieves a shallow maximum at a unit-cell active width of approximately 7 mm. When the cell width is small (below 7 mm in this example), increasing the width produces more total current. However, as the current increases the ohmic and concentration polarization also increases. At sufficiently large unit-cell active width, the increased polarization causes the net current to begin decreasing. Of course, the width at which the maximum current is reached depends upon details of the cell architecture and materials properties. Transport polarization through the nominal support structure considered here has a relatively small effect on performance.

Fig. 7b illustrates that the current density normalized by total width of the unit cell i_{total}. This current density is maximum at a unit-cell active width of approximately 1 mm. Because the interconnect structures are assumed to have fixed dimensions, the fraction of active width compared to the unit-cell width decreases as the unit-cell width decreases (i.e., the interconnect region occupies a larger fraction of the unit-cell width). At very small unit-cell active width, i_{total} is small because a large fraction of the total unit-cell active width is occupied by interconnect. At large unit-cell active width, i_{total} decreases because ohmic, activation, and concentration polarizations increase as total current increases. Although the current increases with decreasing voltage, the positions of the current maxima are affected only weakly by the cell operating voltage. When high power density for a module is the important consideration, i_{total} is a valuable measure of performance.

Fig. 7c illustrates the current density normalized by the active width i_{active}. Because the interconnect region is excluded, this measure of current density does not have a maximum. As the unit-cell active width increases, polarizations associated with increasing total current reduce the current density. At large unit-cell active widths, the two current-density measures (i_{total} and i_{active}) converge toward the same values. This is because the interconnect region occupies a smaller relative fraction of the unit-cell width.

Fig. 8 illustrates the results of a study that is analogous to that shown in Fig. 7. In this case, the interconnect conductivity is increased from σ = 1 S cm^{-1} (typical of an electron-conducting perovskite) to $\sigma = 5 \times 10^4$ S cm^{-1} (typical of a noble metal). Increasing the interconnect conductivity significantly increases the cell performance in the sense that net current is significantly increased. However, the position of the maximum in total current I is only weakly affected. The current density normalized by total width i_{total} is increased to a unit-cell active width of approximately 1.5 mm.

Although the present simulations are based upon assuming isothermal operation, the local heating rates are evaluated. With an interconnect conductivity of σ = 1 S cm^{-1} the local maximum heating rate within the interconnect for the solution shown in Fig. 4 can reach approximately 2 kW cm^{-3}. If the interconnect conductivity is increased to $\sigma = 5 \times 10^4$ S cm^{-1} the local maximum heating rate is greatly reduced to approximately 100 W cm^{-3}.

4.2.2. Cathode current collection

The electrical conductivity of the cathode current-collection layer has a large influence on cell performance. Although LSM is

a relatively poor electronic conductor, the LSM current-collection layer greatly facilitates lateral electron flux relative to the LSM–YSZ structure (Fig. 4). Fig. 9 shows the results of a study that is analogous to those in Figs. 8 and 7, where the LSM conductivity is increased by a factor of ten. Although it may not be clear how to accomplish such an increased conductivity in practice, it is clear the cell performance would benefit greatly by increasing the conductivity of the cathode current collection layer.

4.2.3. Fuel dilution

Within a full module (e.g., Fig. 1) each unit cell is exposed to a different fuel composition. Along the flow direction, the fuel stream is degraded by consumption of the active fuels (e.g., H_2 and CO) and introduction of product species (e.g., H_2O and CO_2). Fig. 10 illustrates how the optimal cell width varies as a function of fuel composition. Although the cell performance is significantly degraded as the fuel is consumed and diluted, the optimal cell geometry width is only weakly affected by fuel composition. This means that the same optimal unit-cell structure can be used for the entire module, thus optimizing the module performance.

5. Summary and conclusions

A two-dimensional computational model has been developed to represent the transport and chemistry throughout a unit cell of an SIS-SOFC module. Distributed electrochemical charge transfer proceeds throughout the composite electrode structures, with Butler–Volmer charge-transfer rates depending upon the local gas-phase composition and electric-potential differences between electrode and electrolyte phases. Reforming chemistry within the anode structure is represented in terms of a multi-step, elementary, reaction mechanism. The model can be applied to evaluate alternative cell architectures and materials properties.

Example problems are used to illustrate important aspects of the SIS performance. The chemical and electrochemical behavior is found to be nearly one-dimensional in the active regions where the dense electrolyte is sandwiched between a cathode and anode structure. That is to say, profiles of species mole fractions and electric potentials depend primarily upon position normal to the dense electrolyte, but weakly upon the position between the cathode and anode interconnectors. In the vicinity of the interconnect structures, however, there is strong two-dimensional behavior as the electronic current is channeled through the interconnection between lateral cells. Indeed, these regions of high electrical current density deserve critical design consideration, seeking to mitigate local damage mechanisms.

The results show that there are optimal cell dimensions that maximize alternative measures of cell performance. Increasing the electrical conductivities of the interconnect structure and the cathode current-collection layer have a significant beneficial influence upon cell performance.

Acknowledgements

We gratefully acknowledge Prof. Scott Barnett (Northwestern University) for sharing his insights and experiences in the development of SIS systems. We are also grateful for insightful discussions with our colleague Prof. Neal Sullivan who is developing new printing techniques to fabricate small-scale SIS structures. This work was supported by a DoD Research Tools Consortium (RTC) program administered by the Office of Naval Research under Grant N00014-05-1-0339.

References

[1] A.O. Isenberg, Solid State Ionics 3/4 (1981) 431–437.
[2] W. Feduska, A.O. Isenberg, J. Power Sources 10 (1983) 89–102.
[3] N.Q. Minh, J. Am. Ceram. Soc. 76 (1993) 563–588.
[4] K. Tomida, T. Kabata, N. Hisatome, A. Yamashita, H. Tsukuda, S. Ohkuma, T. Kiyabu, ECS Trans. 7 (2007) 173–180.
[5] F.J. Gardner, M.J. Day, N.P. Brandon, M.N. Pashley, M. Cassidy, J. Power Sources 86 (2000) 122–129.
[6] G.D. Agnew, R.D. Collins, M. Jorger, S.H. Pyke, R.P. Travis, ECS Trans. 7 (2007) 105–111.
[7] Y. Bai, J. Liu, C. Wang, Int. J. Hydrogen Energy 34 (2009) 7311–7315.
[8] Y. Bai, C. Wang, J. Ding, C. Jin, J. Liu, J. Power Sources 195 (2010) 3882–3886.
[9] T.S. Lai, S.A. Barnett, J. Power Sources 147 (2005) 85–94.
[10] Z. Zhan, S.A. Barnett, Solid State Ionics 176 (2005) 871–879.
[11] T.S. Lai, S.A. Barnett, J. Power Sources 164 (2007) 742–745.
[12] M.R. Pillai, D. Gostovic, I. Kim, S.A. Barnett, J. Power Sources 163 (2007) 960–965.
[13] Y. Lin, Z. Zhan, S.A. Barnett, J. Power Sources 158 (2006) 1313–1316.
[14] H. Zhu, A.M. Colclasure, R.J. Kee, Y. Lin, S.A. Barnett, J. Power Sources 161 (2006) 413–419.
[15] B.A. Haberman, J.B. Young, Int. J. Heat Mass Transfer 47 (2004) 3617–3629.
[16] B.A. Haberman, J.B. Young, J. Fuel Cell Sci. Technol. 3 (2006) 312–321.
[17] B.A. Haberman, J.B. Young, J. Fuel Cell Sci. Technol. 5 (2008) 1–12.
[18] P. Costamagna, A. Selimovic, M.D. Borghi, G. Agnew, Chem. Eng. J. 102 (2004) 61–69.
[19] L. Repetto, G. Agnew, A.D. Borghi, F.D. Benedetto, P. Costamagna, J. Fuel Cell Sci. Technol. 4 (2007) 413–417.
[20] D. Cui, M. Cheng, J. Power Sources 195 (2010) 1435–1440.
[21] H. Zhu, R.J. Kee, J. Electrochem. Soc. 155 (2008) B715–B729.
[22] E.A. Mason, A.P. Malinauskas, Gas Transport in Porous Media: The Dusty-Gas Model, American Elsevier, New York, 1983.
[23] H. Zhu, R.J. Kee, V.M. Janardhanan, O. Deutschmann, D.G. Goodwin, J. Electrochem. Soc. 152 (2005) A2427–A2440.
[24] E.S. Hecht, G.K. Gupta, H. Zhu, A.M. Dean, R.J. Kee, L. Maier, O. Deutschmann, Appl. Catal. A 295 (2005) 40–51.
[25] V.M. Janardhanan, O. Deutschmann, J. Power Sources 162 (2006) 1192–1202.
[26] O. Deutschmann, R. Schwiedernoch, L.I. Maier, D. Chatterjee, Stud. Surf. Sci. Catal. 136 (2001) 215–258.
[27] D. Chen, Z. Lin, H. Zhu, R.J. Kee, J. Power Sources 191 (2009) 240–252.
[28] J. Sanyal, G.M. Goldin, H. Zhu, R.J. Kee, J. Power Sources 195 (2010) 6671–6679.
[29] M. Vogler, A. Bieberle-Hütter, L. Gauckler, J. Warnatz, W.G. Bessler, J. Electrochem. Soc. 156 (2009) B663–B672.
[30] W.G. Bessler, S. Gewies, M. Vogler, Electrochim. Acta 53 (2007) 1782–1800.
[31] W.G. Bessler, J. Warnatz, D.G. Goodwin, Solid State Ionics 177 (2007) 3371–3383.
[32] D.G. Goodwin, H. Zhu, A.M. Colclasure, R.J. Kee, J. Electrochem. Soc. 156 (2009) B1004–B1021.
[33] C.J. Moyer, N.P. Sullivan, H. Zhu, R.J. Kee, J. Electrochem. Soc. 158 (2011) B117–B131.
[34] Y. Saad, Iterative Methods for Sparse Linear Systems, Society of Industrial and Applied Mathematics, Philadelphia, PA, 2003.
[35] P. Deuflhard, E. Hairer, J. Zugck, Num. Math. 51 (1987) 501–516.
[36] R.J. Kee, M.E. Coltrin, P. Glarborg, Chemically Reacting Flow: Theory and Practice, John Wiley, New Jersey, 2003.